Research Article

Simulation of the Uniaxial Mechanical Properties and Crack Evolution of Coal Pillar-Artificial Dam in Abandoned Mines

Xin Lyu [ID],[1] Ke Yang [ID],[2] Juejing Fang [ID],[1] Minke Duan [ID],[1] and Jinzhou Tang[1,3]

[1]*State Key Laboratory of Mining Response and Disaster Prevention and Control in Deep Coal Mines,*
Anhui University of Science and Technology, Huainan 232001, China
[2]*Institute of Energy, Hefei Comprehensive National Science Center, Hefei 230031, China*
[3]*Guizhou Provincial Key Laboratory of Rock and Soil Mechanics and Engineering Safety, Guizhou University, Guiyang,*
Guizhou 550025, China

Correspondence should be addressed to Juejing Fang; juejing_fang@foxmail.com

The key to the construction of underground reservoirs in abandoned mines is the construction of coal pillar-artificial dams, and the choice of bonding parameters between the coal pillars and artificial dams is the deciding factor that determines the engineering stability. Based on the analysis of the force state of coal pillar-artificial dams, the influence of the interface angle was analyzed. Seven sets of coal pillar-artificial dam specimens were prepared and a PFC^{3D} numerical model was constructed to carry out the uniaxial compression test without lateral pressure. Based on the strength, deformation, and energy evolution characteristics of the coal pillar-artificial dam, the influence of the angle of the coal pillar-artificial dam interface on the performance of the specimen was analyzed. The research results showed that the force state of the coal pillar-artificial dam can be divided into three types. The composite simulation curve showed obvious postpeak viscosity. The compressive strength, peak strain, and average dissipated energy curves of the coal pillar-artificial dam showed a unimodal trend that first increased and then decreased. The total energy and elastic energy of the coal pillar-artificial dam showed an increasing trend during loading. The simulated initiation stress and damage stress of the coal pillar-artificial dam specimens were intermediate to that of the coal pillars and the artificial dams, which first increased and then decreased with the increase in inclination, reaching the peak at 70°.

1. Introduction

The Fourteenth Five-Year Plan focuses clearly on increasing the concentration of coal production in resource-rich areas. As outdated coal production units are phased out, the number of closed/abandoned coal mines will continue to rise [1–3]. In this context, it is pertinent to develop overall strategies, basic theoretical research, and key technological breakthroughs for the development and utilization of resources and energy from closed/abandoned mines [4, 5]. In addition, the reuse of the resources contained in abandoned mines and underground spaces plays a vital role in the optimization and sustainable development of the industrial structure of coal enterprises [6]. The construction of underground reservoirs in coal mines provides a realistic basis for innovative ideas such as using abandoned mines to build

pumped-storage power stations [7]. The construction of abandoned mines pumped-storage power stations can improve the integration of China's power source network and load storage, facilitating the establishment of a clean energy base with multiple complementary energy sources. [8]. The construction of safe and controllable underground reservoirs has important experimental and practical value for the protection of groundwater resources and the development and utilization of subterranean space in closed/abandoned mines [9]. To this end, many researchers have studied the safety and stability of the reuse of subterranean spaces in abandoned mines [10–13] and established a stability evaluation system for water storage systems in underground mines. Case evaluations for the structural stability of underground reservoirs in coal mines were also carried out [14, 15].

At the same time, the researchers also carried out a series of experimental studies on various parameters of the underground reservoir dam. Artificial dams were constructed to study the dynamic failure characteristics under different intensity conditions, and studies on the comprehensive strength measurement of ultrasonic rebound, cyclic loading, and uniaxial compression acoustic emission test were carried out [16, 17]. The seismic performance and dynamic response [14, 18] were tested, based on which a fuzzy multilevel comprehensive evaluation model for the safety of artificial dams was proposed [20]. The FLAC^{3D} numerical simulation software was used to establish an artificial dam model, on which graded water pressure was applied to study the water-rock migration interaction [21–23]. The limiting water head value that the artificial dam can bear, and the vulnerable position were determined, [24, 25] and the fluid-solid coupling numerical model of the underground reservoir under the coupled action of mining and flooding was constructed [16]. Through underground sampling, the rock fragmentation characteristics [27] and size effect test were carried out to analyze the deformation behavior of underwater coal and rock [28, 29]. Some researchers have also carried out the mechanical characteristics testing of coal-rock composite as per the existing state of coal-rock in the mine, [27] analyzing the deformation behaviors and individual characteristics of the coal-rock composite [31], [32] to understand the characteristics of damage and failure of the composite as well as progressive instability [33], [34]. Based on existing data regarding underground reservoirs, the dam thickness was optimized, [35] and the stability of the coal pillar-artificial dam connection was simulated [36–38]. These studies focus mainly on the analysis of the coal-rock-artificial dam structure, and the composite structure is considered only with respect to the plane bonding. However, the construction of the abandoned coal pillar-artificial dam is not a simple plane bonding process. Research on the instability characteristics of the bonded structure in the composite state is of great significance to the utilization of underground space in abandoned mines.

Considering the bonding angle as the research object, seven sets of coal pillar-artificial dam type coal-rock specimens were prepared and a PFC^{3D} numerical model was constructed. A uniaxial compression test was carried out without lateral pressure. Based on the strength, deformation, and energy evolution characteristics of coal pillar-artificial dams, the influence of the angle of the coal pillar-artificial dam on the performance of the specimen was analyzed. The PFC^{3D} model was used to explore the crack evolution, particle displacement, and spatial distribution behaviors, based on which the bonding structure of the water storage dam in the underground space of the abandoned mine was optimized.

2. Deformation Mechanics Analysis of Coal Pillar-Artificial Dam

2.1. Stress State of Coal Pillar-Artificial Dam. Different from complete coal seams or rock formations, coal pillar-artificial dams are composed of two different media, which differ significantly from the single structure when they are loaded. When bonding them to each other, it is necessary to consider not only the strength of the artificial dam, but also the coordinated bearing capacity of the remaining coal pillars. The interaction between the two media restricts each other and carries the load together. The tightness of the bond between the two media determines the stress state under loading (Figure 1).

(1) When the coal pillars and artificial dam are loosely bonded (Figure 1(a)), they are subjected to their respective loads, and stress concentration is easily formed at the interface. The stress states of the single structure on both sides are unidirectional, and they will break when each side reaches the critical value. At the same time, the damage on one side aggravates the damage on the other side.

(2) When the coal pillar-artificial dam bond is tight (Figure 1(b)), the amount of deformation of the coal pillar is larger due to its relatively weak physical properties as it is influenced by the structural change of the other side caused by stress. As a result, the unilateral bearing capacity of the composite is increased, with the coal pillar being subjected to bidirectional stress and the artificial dam being subjected to unidirectional stress.

(3) When the coal pillar-artificial dam is extremely tightly bonded (Figure 1(c)), the two will carry the load in a coordinated manner. The coal pillars share the deformation while transferring part of the stress to the side of the artificial dam, resulting in a unidirectional stress of the overall structure with a stable internal structure.

2.2. Mechanical Model of Coal Pillar-Artificial Dam. The coal pillar-artificial dam is composed of a coal pillar side and an artificial dam side, both of which are elastoplastic bodies that can be represented by Saint-Venant bodies (Figure 2).

At the same time, the elastomer part can be refined based on different lithologies. That is, the dual strain Hooke's law is applied with the coal pillar approximated as the soft part and the artificial dam as the hard part, which satisfies the Hooke's law, respectively. In addition, the mechanical components on the coal pillar side and the artificial dam side are connected in parallel according to the bonding method of the coal pillar-artificial dam.

$$\begin{cases} \sigma = \sigma_1 + \sigma_2, \\ \epsilon = \epsilon_1 = \epsilon_2. \end{cases} \tag{1}$$

The change of the overall strain of the composite considers the deformation of the single bodies on both sides, and there is also the influence of interface bonding. Therefore, the combined body will be deformed under the action of the external force; however, due to the difference of σ_S of the two sides and the different degrees of bonding, different mechanical models may be suitable for use:
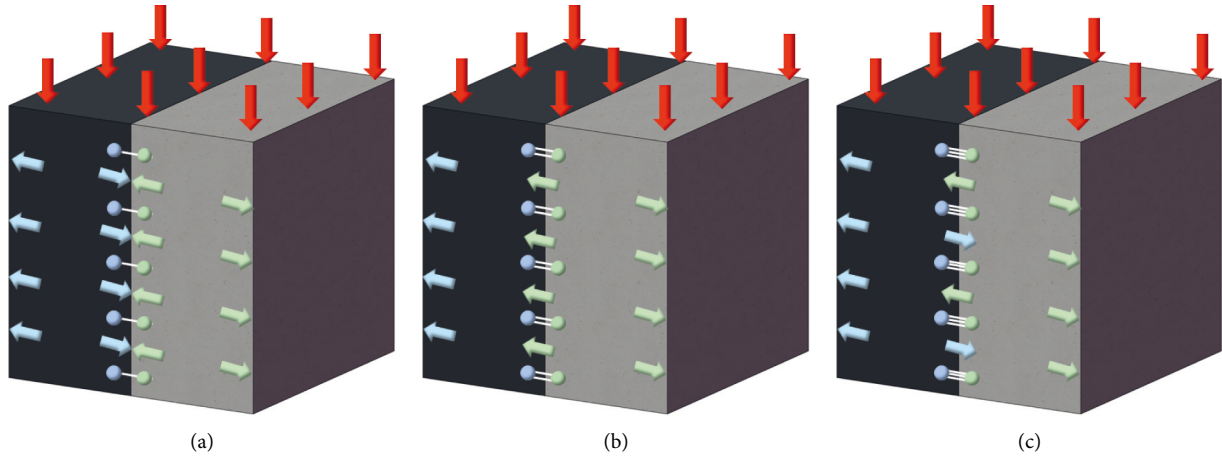
FIGURE 1: Stress state of coal pillar-artificial dam. (a) Split bearing, (b) shared bearing, and (c) coordinated bearing.
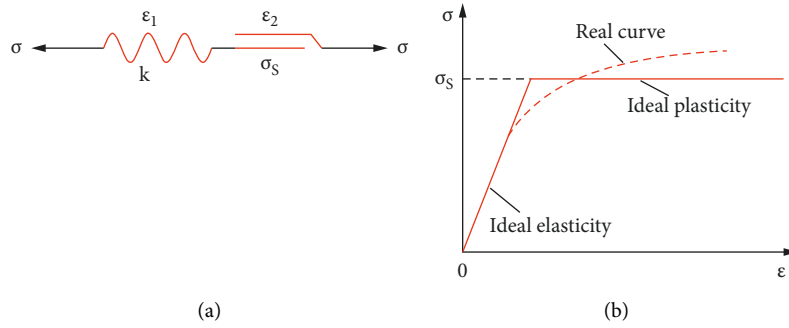

FIGURE 2: Schematic diagram of the constitutive relationship of Saint-Venant body. (a) Saint-Venant body mechanical model, (b) schematic diagram of elastoplastic model.

2.2.1. Split Loading Constitutive Model of Coal Pillar-Artificial Dam.

$$\begin{cases} \sigma_1 < \sigma_{S_1}, \epsilon = \dfrac{\sigma_1}{k_1} = \dfrac{\sigma_2}{k_2}, \\ \\ \sigma_1 \geq \sigma_{S_1}, \epsilon \longrightarrow \infty, \end{cases} \tag{2}$$

where σ_1 and σ_2 are the stresses applied to the coal pillar side and the artificial dam side, respectively. The terms k_1 and k_2 are the elastic coefficients of coal pillars and artificial dams, σ_{S_1} and σ_{S_2} are the frictional resistance between the coal pillar side and the friction plate of the artificial dam, and m is the frictional resistance correction factor, with $\sigma_{S_1} + \sigma_{S_2}/m > \sigma_{S_2}$.

When the combined body is loosely bonded, the strain is dominated by the deformation of the coal pillar side. When σ_1 is smaller than the friction resistance σ_{S_1} of the friction plate on the side of the coal pillar, the combined body will be elastically deformed. At the same time, as $k_1 < k_2$ then $\sigma_1 < \sigma_2$. The artificial dam side inside the combined body bears most of the stress and maintains a complete structure. When $\sigma_1 \geq \sigma_{S_1}$, the deformation of the coal pillar side cannot be controlled, and the stress on the other side increases instantaneously with the failure of one side, leading to an overall stable structure.

2.2.2. Shared Loading Constitutive Model of Coal Pillar-Artificial Dam.

$$\begin{cases} \sigma_2 < \sigma_{S_2}, \epsilon = \dfrac{\sigma_1}{k_1} = \dfrac{\sigma_2}{k_2}, \\ \\ \sigma_2 \geq \sigma_{S_2}, \epsilon \longrightarrow \infty. \end{cases} \tag{3}$$

When the combined body is tightly bonded, the stress in the coal pillar-artificial dam is dominated by the artificial dam side. At this time, the friction resistance of the friction plate σ_{S_2} shall prevail. Under the action of the external force, the combined body deforms elastically. At the same time, σ_2/σ gradually increases with the increase in the external load, and the overall deformation is in a controllable range. When $\sigma_2 \geq \sigma_{S_2}$, damage and deformation occur on the artificial dam side, and the overall structure becomes unstable.

2.2.3. Coordinated Loading Constitutive Model of Coal Pillar-Artificial Dam.

$$\begin{cases} \sigma < \dfrac{\sigma_{S_1} + \sigma_{S_2}}{m}, \epsilon = \dfrac{\sigma_1}{k_1} = \dfrac{\sigma_2}{k_2}, \\ \\ \sigma \geq \dfrac{\sigma_{S_1} + \sigma_{S_2}}{m}, \epsilon \longrightarrow \infty. \end{cases} \tag{4}$$

When the combined body is extremely tightly bonded, the external load is carried together by the two parts. In such a situation, the friction resistance of the integrated body friction plate $\sigma_{S_1} + \sigma_{S_2}/m$ shall prevail, where the value of m depends on the bonding structure parameters of the two sides. Here, the overall frictional resistance of the combined body increases, which improves the overall load-bearing and deformation capacity until $\sigma \geq \sigma_{S_1} + \sigma_{S_2}/m$, where the overall structure of coal pillar-artificial dam is unstable and damaged.

3. Experiment and Numerical Modeling

3.1. Experiment Setup.
The combined body specimen of this test is composed of two parts: coal pillar and artificial dam. Because the lithology of natural coal is relatively brittle and not suitable for processing, the coal pillar was made of coal powder and cement in a mass ratio of cement: coal powder: water = 1 : 2.5 : 1. The artificial dam was made by mixing river sand and cement, the mass ratio of which was cement: river sand: water = 1 : 1.5 : 0.5 where the sieving size of coal powder was 2.0 mm × 2.0 mm and the sieving size of river sand was 2.5 mm × 2.5 mm, as shown in Figure 3 (the material ratio was selected according to the existing literature).

Since the connection between the coal pillar and the artificial dam was a trapezoidal connection, it involved three factors: angle, width, and depth. This test focused on the impact of mechanical properties caused by angle changes (Table 1 and Figure 4). The width was fixed to 30 mm and the depth was fixed to 7.5 mm, resulting in a total of seven groups (including five coal pillars-artificial dam specimens, one coal pillar specimen, and one artificial dam single specimen) [30]. Each group had three test pieces, named according to the number angle (such as A-80°). The test pieces were cylinders with a size of Φ50 mm × L100 mm, all of which were taken from a large cubical test block.

The large cube test block was shaped by the model steel plate in the mold. The coal pillar part was poured first, and the steel plate was taken out after the vibration was completed, after which the artificial dam part was poured. After vibrating, the test block was left to stand for 48 h prior to demolding. After the large cube test block has been cured to 28 days under natural conditions, the core was extracted in a direction to the interface (Figure 5). The unevenness of both ends was polished with fine sand to ensure that the unevenness did not exceed 0.05 mm, and the nonperpendicularity of each adjacent surface did not exceed ±0.5°.

A rock mechanics testing machine was used to perform the uniaxial compression test without lateral pressure on the test pieces (Figure 6):

(1) The test piece was placed on the lower platen of the test machine. The center of the test piece was aligned with the center of the lower platen of the test machine, and a digital dial gauge was installed to connect to the computer system for debugging.

(2) The upper platen of the machine was lowered until it barely touched the test piece. At the same time, the axis of the test piece was kept coincident with the loading center line of the testing machine to avoid an eccentric force, which will affect the test results.

(3) A high-definition camera was set up. The loading rate and displacement acquisition frequency were set to be 0.1 kN/s and 100 ms, respectively. The sample was subjected to axial stress until the test piece was finally destroyed.

(4) The data collected in the experiment were recorded and saved for analysis and processing.

3.2. Model Establishment and Parameter Calibration.
The PFC particle discrete element starts from the mesoscale, and does not need to assume a macroscopic constitutive model of the material, but analyzes the propagation and failure process of rock microcracks from the microscopic level, and establishes the macroscopic and microscopic correspondence of the rock. From the microlevel, the rock is formed by the bonding of tiny mineral particles inside, and the arrangement of its components affects the development characteristics of the microcrack system inside the rock. The bonding medium between the particles has different contact relations, controlled by a certain fracture criterion, and its deformation and strength parameters have different degrees of dispersion. These many microscopic factors all affect the macroscopic mechanical properties of the rock to a certain extent. Express. Compared with the traditional finite element, the discrete element has the following advantages: the microparticle model can reflect the process of microcracks in the rock propagating into macro-cracks, reflecting the mutual influence of the cracks in the process of propagation, and the redistribution of the contact force between particles. A microscopic particle model that accurately reflects the characteristics of the rock is constructed, which can reasonably simulate the dynamic fracture process of the rock microstructure. In order to study the crack evolution characteristics of the coal pillar-artificial dam from a mesoscopic perspective, based on the particle flow theory, the PFC³ᴰ software was used to numerically simulate the uniaxial compression of the specimen.

The particle discrete element method is developed based on the discrete element theory of Cundall et al. It uses an explicit difference algorithm to alternately use the force-displacement law and Newton's law of motion in the calculation cycle, and update the contact force between contacting particles through the force-displacement law. The position of the particles is updated through the law of motion to form a new contact of the particles, thereby simulating the movement and interaction process of the particles. There are many types of bonding models built in the PFC. Here, a parallel bonding model is selected (Linearpbond), which is more suitable for simulating hard rock materials. The Linearpbond model can transmit force and moment. When the applied stress exceeds the bond strength, the bond of the parallel bond model will be broken. It is determined that the size of the simulated test piece is a cylinder of Φ50 mm × L100 mm, and the upper and lower
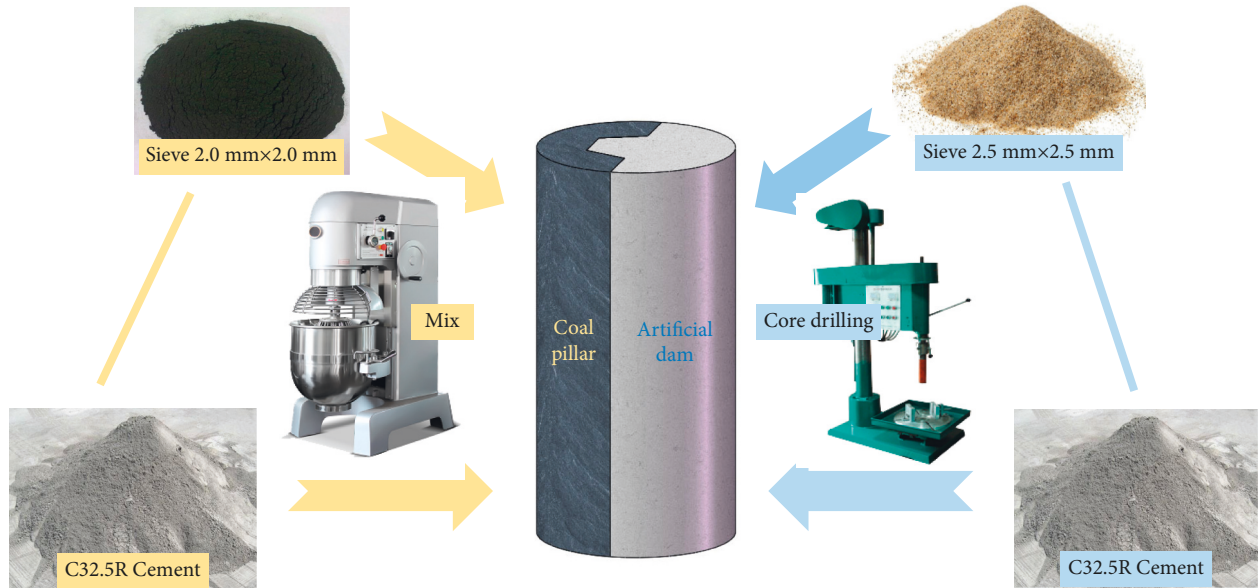
Figure 3: Sample preparation process.

Table 1: Test parameter design.

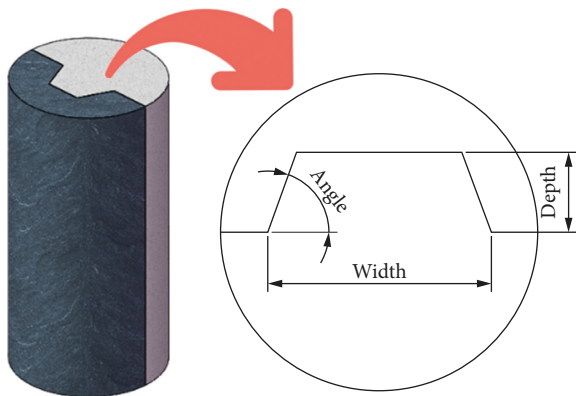| Factor	Angle (°)	Width (mm)	Depth (mm)
	50	30	7.5
	60	30	7.5
Gradient	70	30	7.5
	80	30	7.5
	90	30	7.5

Figure 4: Structure of the coal pillars-artificial dam.

end faces are calculated with rigid walls, and the surrounding is a free boundary (Figure 7).

The microparameter calibration of numerical calculation involves tuning to obtain reasonable microparameters by the trial-and-error method based on the macro-parameters. That is, before the numerical calculation, micromechanical parameters are assigned to the model. Then, the calculated macromechanical parameters of the material are compared with the measured experimental values. The corresponding micromechanical parameters are varied to calibrate the macro-mechanical parameters of the material. When the numerical calculation results are consistent with the experimental results, the model is considered reliable. The material parameter calibration process is shown in Figure 8.

By calibrating the mechanical parameters, the micromechanical parameters of the coal pillar and artificial dam single bodies were obtained, respectively. The parameters can then be substituted into the combined body to calibrate the interface, as shown in Table 2.

The uniaxial compression experiment controlled by displacement loading was simulated by specifying the rates of downward and upward motion of the top and bottom walls of the model, respectively. The friction coefficient between the wall and the particles was set to 0.1 (to eliminate the influence of the end face), and the rate of movement was set to 0.05 m/s. At the same time, to obtain a complete stress–strain curve, loading was stopped when the stress dropped to 70% after the specimen was broken. During this process, the changes in the stress, strain, and number of cracks during the entire loading process were recorded using a code written in Fish.

4. Uniaxial Compression Characteristics of Coal Pillar-Artificial Dams

Through experiment and PFC^{3D} simulations, the stress–strain curves and test data were obtained after uniaxial compression (Figure 9, Table 3). Representative curves in the test group were plotted.

It can be seen from Figure 9 that the experimental data agreed with the simulated data. The small difference between them was due to the denser and more homogeneous particles used in the simulation. In addition, during the experiment, the pressure of the testing machine was released after detecting the damage and so, compared with the numerical simulation curve, it lacks the postpeak variation curve.
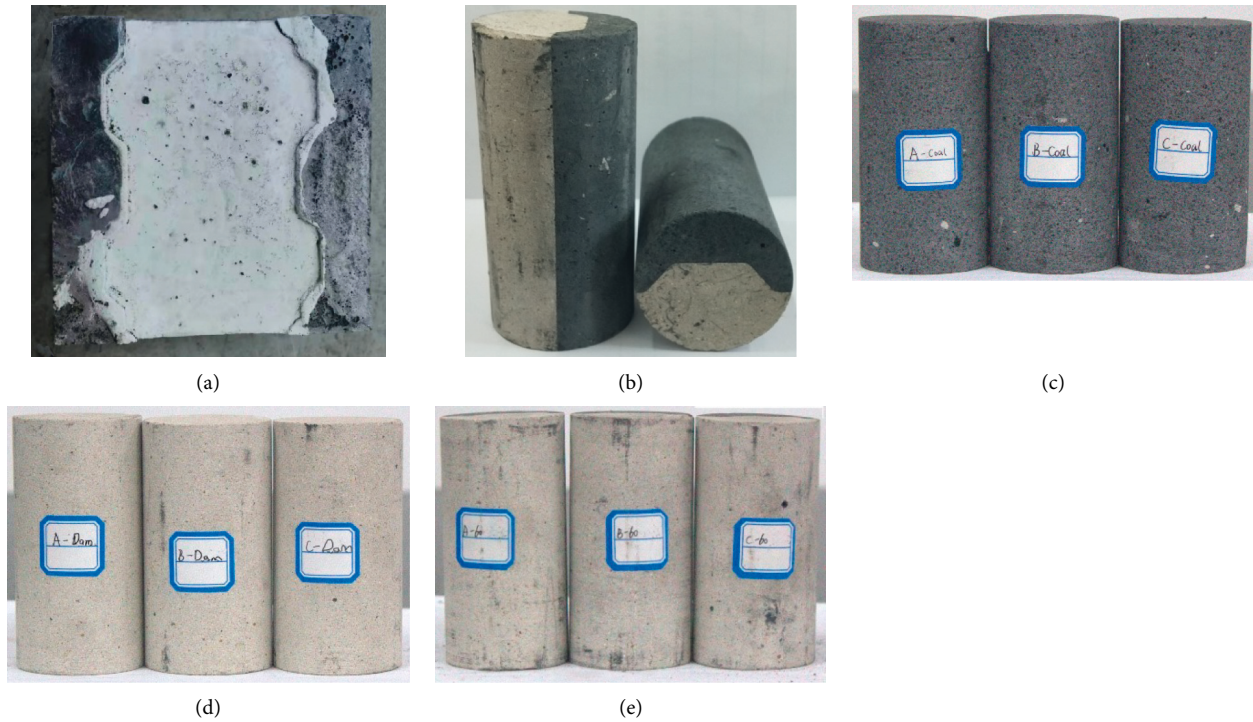
(a)

(b)

(c)

(d)

(e)

FIGURE 5: Coal pillars-artificial dam samples. (a) Cube test block, (b) core drilling of test piece (c) coal pillar samples, (d) artificial dam samples, and (e) coal pillars-artificial samples.
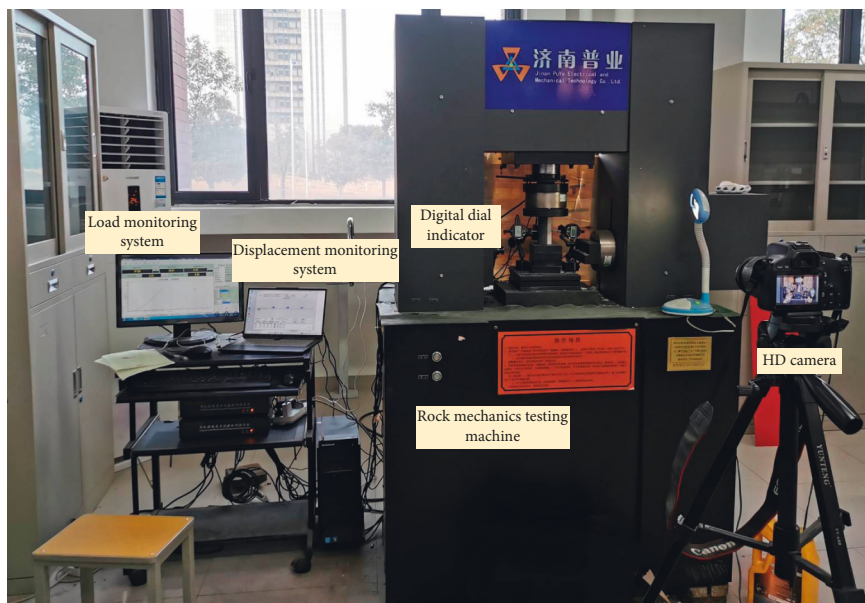

FIGURE 6: Test equipment.

The test curves had the complete five-stage characteristics of original void compaction–linear elasticity–elasto-plastic transition–plasticity–failure, while the simulation curves were monotonous. At the same time, the coal pillar test curves showed a certain postpeak viscosity, which was obvious in the simulation curves of the combined body. It can also be seen that the peak stress and strain of the viscosity curve decreased with the increase in the interface angle, and the distance between the peak compressive strength and the peak of the viscosity curve also decreased gradually with the increase in the inclination. It shows that as the angle increases, the structure of the combined body becomes more complete.

4.1. Analysis of Strength Characteristics of Coal Pillar-Artificial Dam. In order to analyze the coal pillar-artificial dam strength characteristics in depth, combined with the uniaxial
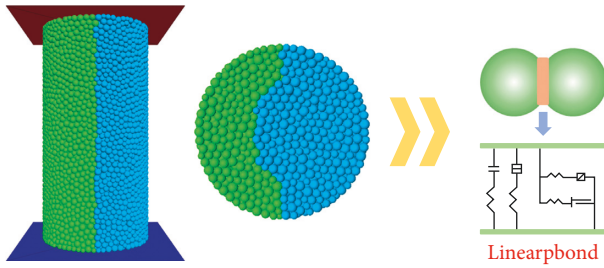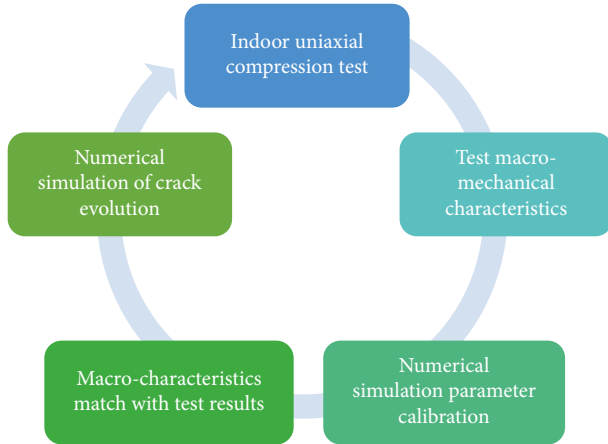
Figure 7: Simulated specimen and bonding model.

Figure 8: Calibration trial and error method.

Table 2: Micromechanical parameters of the numerical model.

Type	Name	Value
Coal pillar	Particle radius	1.0~1.5 mm
	Friction coefficient	0.4
	Effective modulus	0.4 GPa
	Normal stiffness	1.7 MPa
	Tangential stiffness	3.4 MPa
Interface	Particle radius	1.0~1.5 mm
	Friction coefficient	0.4
	Effective modulus	2 GPa
	Normal stiffness	6 MPa
	Tangential stiffness	12 MPa
Artificial dam	Particle radius	1.0~1.5 mm
	Friction coefficient	0.4
	Effective modulus	2 GPa
	Normal stiffness	10 MPa
	Tangential stiffness	20 MPa

compression laboratory test results, the relationship curve between the compressive strength of the composite specimen and the angle of the interface is obtained, as shown in Figure 10.

It can be seen that the strength of the composite specimen is mostly between the strength of the coal pillar and the individual strength of the artificial dam. As the angle changes, the average curve of the coal pillar-artificial dam test shows a single-peak change trend that first increases and then decreases. At the same time, the peak point is greater than the compressive strength of the single specimen of the artificial dam, which indicates that the strength of the composite specimen is not only determined by the proportion of the coal pillar and the volume of the artificial dam, but also related to the connection form and the angle of the interface; the reduction after the peak point, both the small rate and the increase rate are slightly larger than before the peak; the angle change of the interface changes the stress transmission conditions in the coal pillar and the artificial dam, thereby affecting the stress state of the two, and finally shows a clear difference.

Compared with the single body artificial dam, the compressive strength of the coal pillar-artificial dam was reduced by 8.16%, 5.17%, −0.70%, 4.09%, and 8.01% during the process of increasing the bonding angle of coal pillar-artificial dam from 50° to 90°. Compared with the single body coal pillar specimen, the increase was 498.48%, 517.90%, 556.19%, 524.95%, and 499.43%, respectively.

The test mean curve was fitted using the single-peak GussAmp formula:

$$\sigma_s = 31.36 + 3.11 e^{-\dfrac{(x_s - 70.81)^2}{27.44^2}}, \tag{5}$$

where σ_s is the uniaxial compressive strength of the test piece and x_s is the interface angle of the coal pillar-artificial dam. The correlation coefficient R^2 is 1, indicating that the formula can fully characterize the relationship between the angle and the compressive strength of coal pillar-artificial dam, and can guide the construction of artificial dams on-site.

4.2. Analysis of Deformation Characteristics of Coal Pillar-Artificial Dam. Drawing the relationship between angle and peak strain (Figure 11), it can be seen that the strain of the coal pillar-artificial dam specimen is larger than that of the dam body specimen, and the peak strain of the coal pillar specimen is the smallest. This is due to the combined coal. The column not only has the deformation characteristics of a single unit, but also bears a much higher limit stress than the single unit. The severe deformation greatly increases the strain of the combined body; the average curve of the coal column-artificial dam test shows a single peak that first increases and then decreases, changes trend, and the increase rate before the peak is higher than the increase rate after the peak.

Compared with the single body artificial dam, the peak strain of coal pillar-artificial dam was increased by 12.04%, 12.96%, 14.81%, 11.11%, and 10.19% during the process of increasing the bonding angle of the coal pillar-artificial dam from 50° to 90°. Compared with the single body coal pillar test piece, the increase was 28.72%, 29.79%, 31.91%, 27.66%, and 26.60%, respectively. In the coal pillar-artificial dam test piece, the deformation of the pillars was shared by the coal pillar; therefore, the total deformation was much higher than that of the single body artificial dam test piece.

The mean curve from the test is fitted using the single-peak Laplace formula:
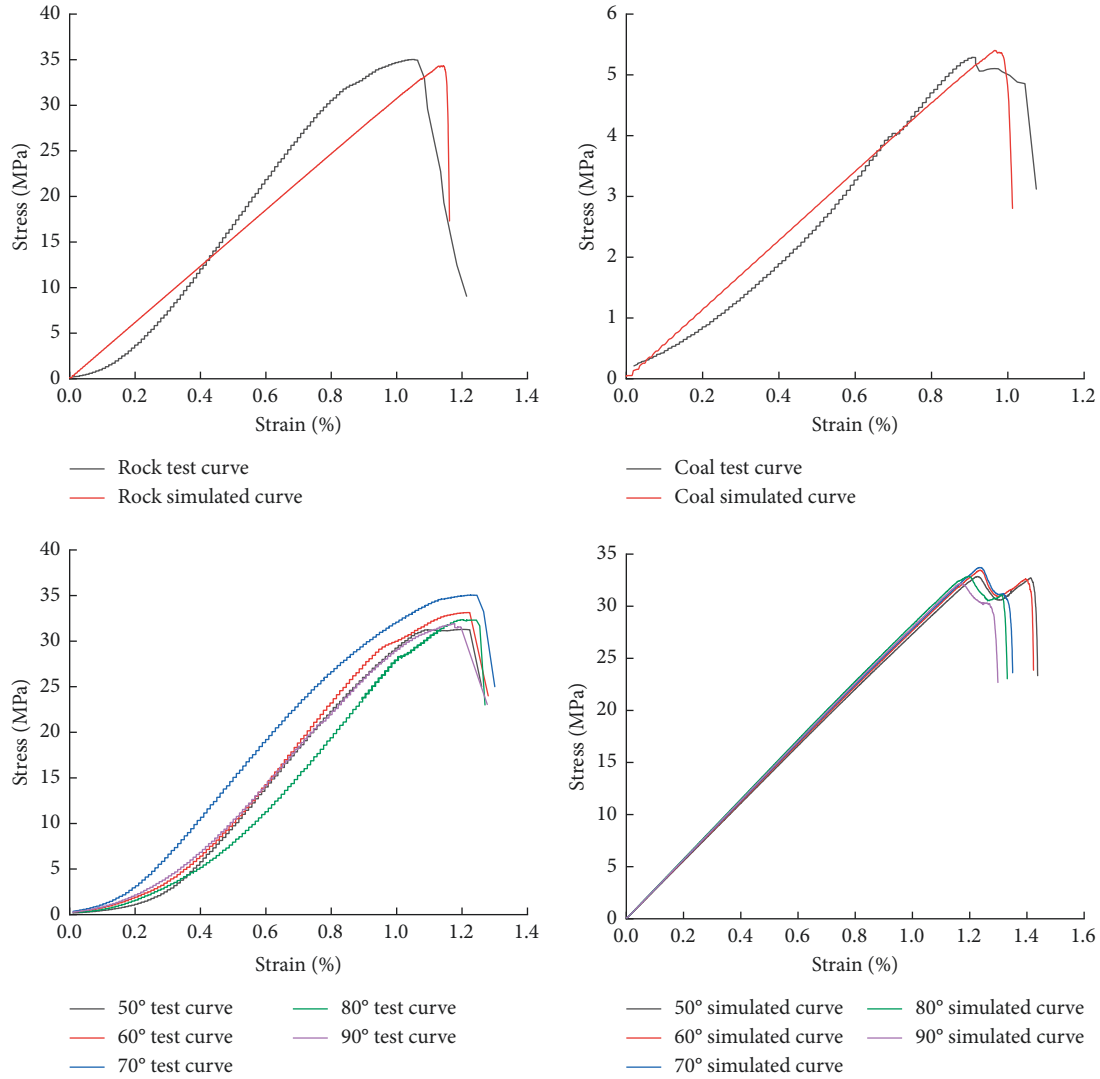
Figure 9: Test and simulated stress–strain curves.

Table 3: Test and simulation results.

Serial number	Test		Simulation	
	Mean stress (MPa)	Mean strain (%)	Stress (MPa)	Strain (%)
Dam	34.21	1.08	34.33	1.14
Coal	5.25	0.94	5.40	0.97
50°	31.42	1.21	32.85	1.23
60°	32.44	1.22	33.46	1.24
70°	34.45	1.24	33.71	1.24
80°	32.81	1.20	32.85	1.20
90°	31.47	1.19	32.20	1.17

$$\epsilon_s = 1.19 + \frac{1}{13.08} e^{-\frac{|x_s - 66.54|}{6.54}}, \tag{6}$$

where ϵ_s is the peak strain of the test piece and x_s is the interface angle of the coal pillar-artificial dam. The correlation coefficient R^2 is 0.79. The formula can characterize the relationship between the angle and the peak strain of coal

pillar-artificial dam and can predict the stability of the site structure.

4.3. Energy Evolution of Coal Pillar-Artificial Dam. The specimen interacts energetically with its surroundings in the form of elastic energy, dissipated energy, surface energy, radiant energy, kinetic energy, thermal energy, etc. At the same time, the energy transfer and transformations of the specimen in the uniaxial loading process are divided into four parts: energy input, energy accumulation, energy dissipation, and energy release. Energy input refers to the mechanical energy supplied by the surroundings. In the test system, it refers to the work done by the test press on the rock. Energy accumulation refers to the elastic deformation energy during the load phase. The energy input from the outside is stored in the test piece in the form of elastic deformation energy. When the external force is removed, the elastic deformation is restored, and the elastic deformation energy is released to the surroundings. Energy dissipation refers to plastic strain energy and surface energy. Because
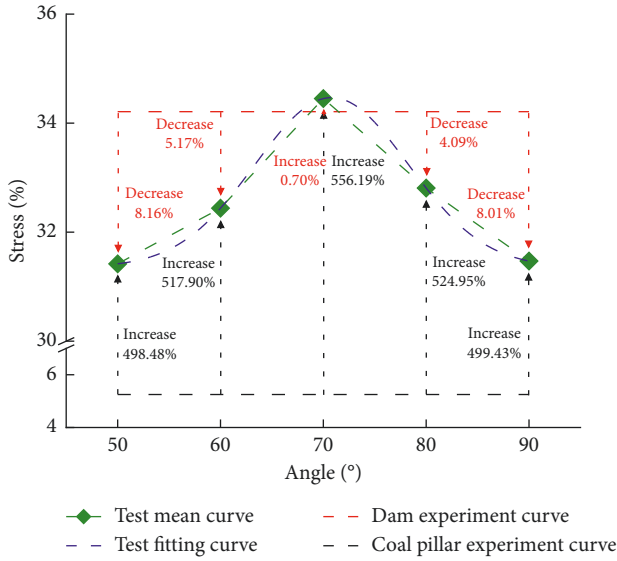
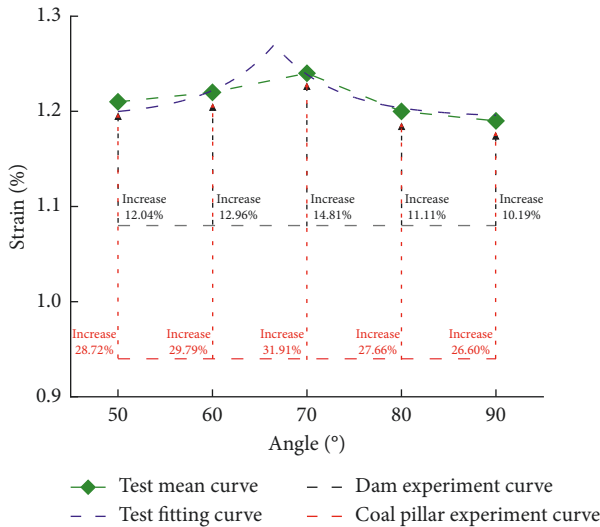FIGURE 10: Relationship between angle and compressive strength.

FIGURE 11: Relationship between angle and peak strain.

FIGURE 12: Schematic diagram of energy evolution relationship.

there are many discontinuous structures such as pores, cracks, and joints inside, under the action of external force, the energy input from the outside will not only bring about elastic deformation, but also produce irreversible plastic deformation, resulting in plastic deformation energy. With the development and expansion of internal microcracks, it also leads to the formation of new microcracks. In damage mechanics, the energy consumed by new cracks in the process of crack propagation is called surface energy. Energy is released as the kinetic energy of splashing and breaking, while acoustic energy, radiant energy, and thermal energy are generated by the instability and destruction due to failure. The energy released during failure comes from the elastic deformation energy accumulated in the early stage.

Energy evolution under uniaxial compression is shown in Figure 12. The coal pillar-artificial dam stress–strain curve peak area represents the work done by the testing machine
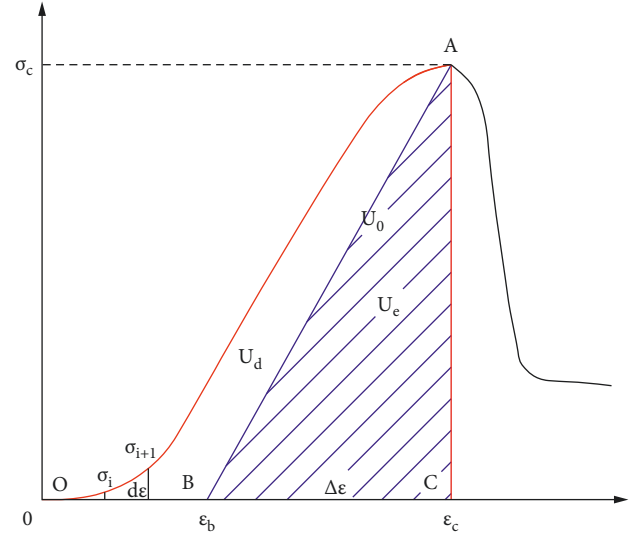
on the sample. Energy input U_o can be represented by the OAC area in Figure 12. A straight line parallel to the stress–strain plot along the peak point, and a straight line perpendicular to the axis at the peak point are drawn. The area of the triangle formed is the accumulated elastic energy U_e (ABC area in Figure 12). The area occupied by OAB shown in Figure 12 is the dissipation energy U_d.

The input energy supplied to the combined body U_o is the sum of elastic energy U_d and dissipated energy U_d.

$$U_o = U_e + U_d, \tag{7}$$

$$U_o = \int_0^{\epsilon_s} \sigma_i d\epsilon, \tag{8}$$

$$U_e = \frac{\sigma_s \Delta \epsilon_s}{2}, \tag{9}$$

where σ_s (MPa) is the peak strength of the coal pillar-artificial dam, $\Delta \epsilon$ is the axial strain difference, ϵ_b and ϵ_c are the stress–strain curve edge nodes.

According to equations (7)–(9), the energy evolution process during each combined loading process can be obtained (Table 4). External energy is continuously input into the coal pillar-artificial dam test piece during the loading process. Part of the energy is transformed into dissipated energy, which is manifested in the plastic deformation of the combined body and microcrack initiation, expansion, and other microdamages. The rest of the energy is stored inside the test piece in the form of elastic energy.

The energy evolution behaviors of coal pillar-artificial dam test pieces with different angles were similar. The A-70° test piece was selected to draw the energy and stress relationship curve.

It can be found from Figure 13 that the total energy and elastic energy increase in the same manner as the stress–strain relationship curve. The rate of increase of the two in the early stage was relatively small, and the curve was relatively flat during the compaction stage of the stress–strain

Table 4: Uniaxial compression energy value of coal pillar-artificial dam test piece.

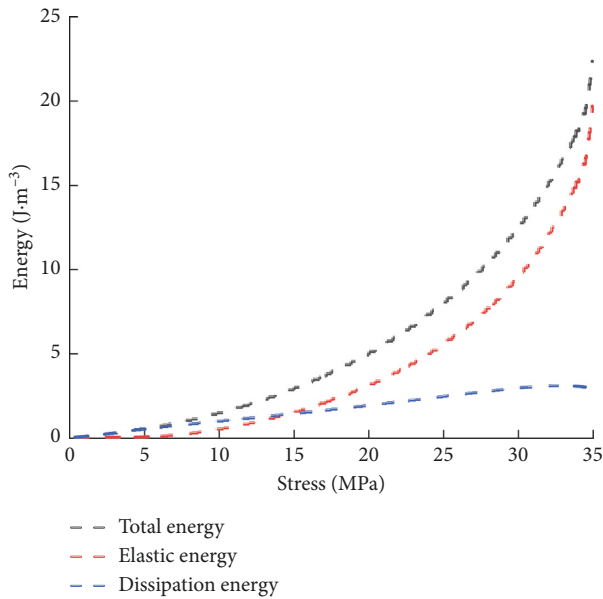| Group	Total energy ($J \cdot m^{-3}$)	Elastic energy ($J \cdot m^{-3}$)	Dissipated energy ($J \cdot m^{-3}$)	Percentage of elastic energy (%)
Dam	18.86	16.26	2.60	86.21
Coal	2.19	2.09	0.10	95.43
50°	17.72	16.76	0.96	94.58
60°	18.93	17.33	1.60	91.55
70°	22.70	20.0	2.62	88.11
80°	16.34	15.14	1.20	92.66
90°	17.44	16.47	0.97	94.44

Figure 13: Relationship between energy and stress (A-70°).

curve, which was followed by a gradual increase in the rate. It can be observed that the total energy and elastic energy increased in a linear manner that corresponds to the elastic stage of the stress–strain curve. When the sample reached the peak stress, the total energy and elastic energy both reached the maximum, and the proportion of elastic energy gradually increased, subsequently starting to release. The internal cracks of the specimen rapidly expanded into macroscopic cracks, which eventually led to the destruction of the specimen. The dissipation energy curve increased obviously in the early stage, then tended to flatten, and finally decayed. It is related to the three stages before the peak of the stress–strain curve. In the initial compaction stage, not only the microcracks in the coal pillar and the artificial dam, but also on the interface between the coal pillar and the artificial dam were compacted. At this time, most of the work done by the testing machine on the sample was converted into work done on the compact structure surface, and the accumulated elastic energy was small. Then, in the elastic phase, almost all the work done by the testing machine was converted into elastic energy. Therefore, the dissipated energy density remained almost unchanged. When entering the prepeak plastic yield stage, the
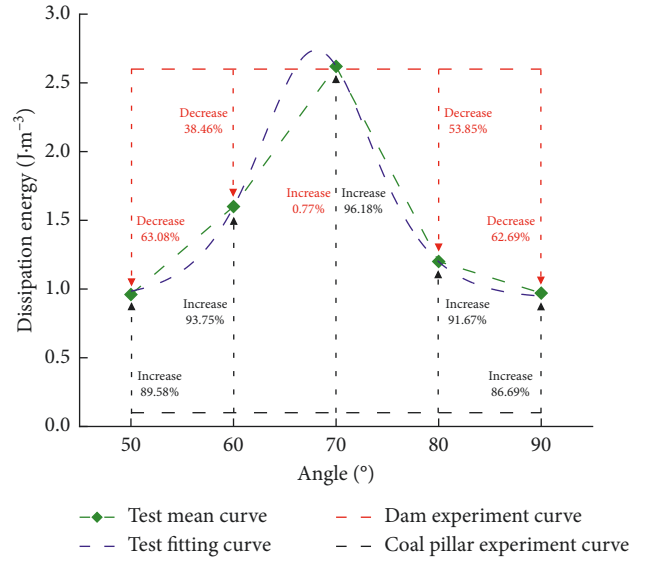

Figure 14: Relationship between angle and dissipated energy.

strength of the sample was close to the peak value and the deformation was reduced. At the same time, the internal energy accumulation entered the peak period, at which time the external radiation energy decreased.

It can be seen from Figure 14 that as the inclination changes, the dissipation energy curve of the combined sample shows a unimodal trend that first increases and then decreases. Like the stress curve, the peak point was greater than the single body specimen of the artificial dam, while the dissipation energy of the single body specimen of the coal pillar was much smaller than other curves.

Compared with the single body artificial dam, the compressive strength of coal pillar-artificial dam specimens was reduced by 63.08%, 38.46%, −0.77%, 53.85%, and 62.69% during the process of increasing the bonding angle from 50° to 90°. Compared with the single body coal pillar specimen, the increase was 89.58%, 93.75%, 96.18%, 91.67%, and 86.69%, respectively.

The test mean curve was fitted using the single-peak Logistpk formula:

$$U_d = 0.93 + \frac{7.24 e^{-x_s - 68.06/3.72}}{\left(1 + e^{-x_s - 68.06/3.72}\right)^2}, \tag{10}$$

where U_d is the peak strain of the test piece and x_s is the interface angle of the coal pillar-artificial dam. The correlation coefficient R^2 is 0.99. The equation can characterize the relationship between the dissipated energy and the peak strain of coal pillar-artificial dam and can provide a basis for on-site safety monitoring.

5. Crack Evolution Study of the Coal Pillar-Artificial Dam

5.1. Analysis of Crack Evolution of the Coal Pillar-Artificial Dam. In the process of simulating the uniaxial compression of coal pillar-artificial dam specimens (Figure 15), the
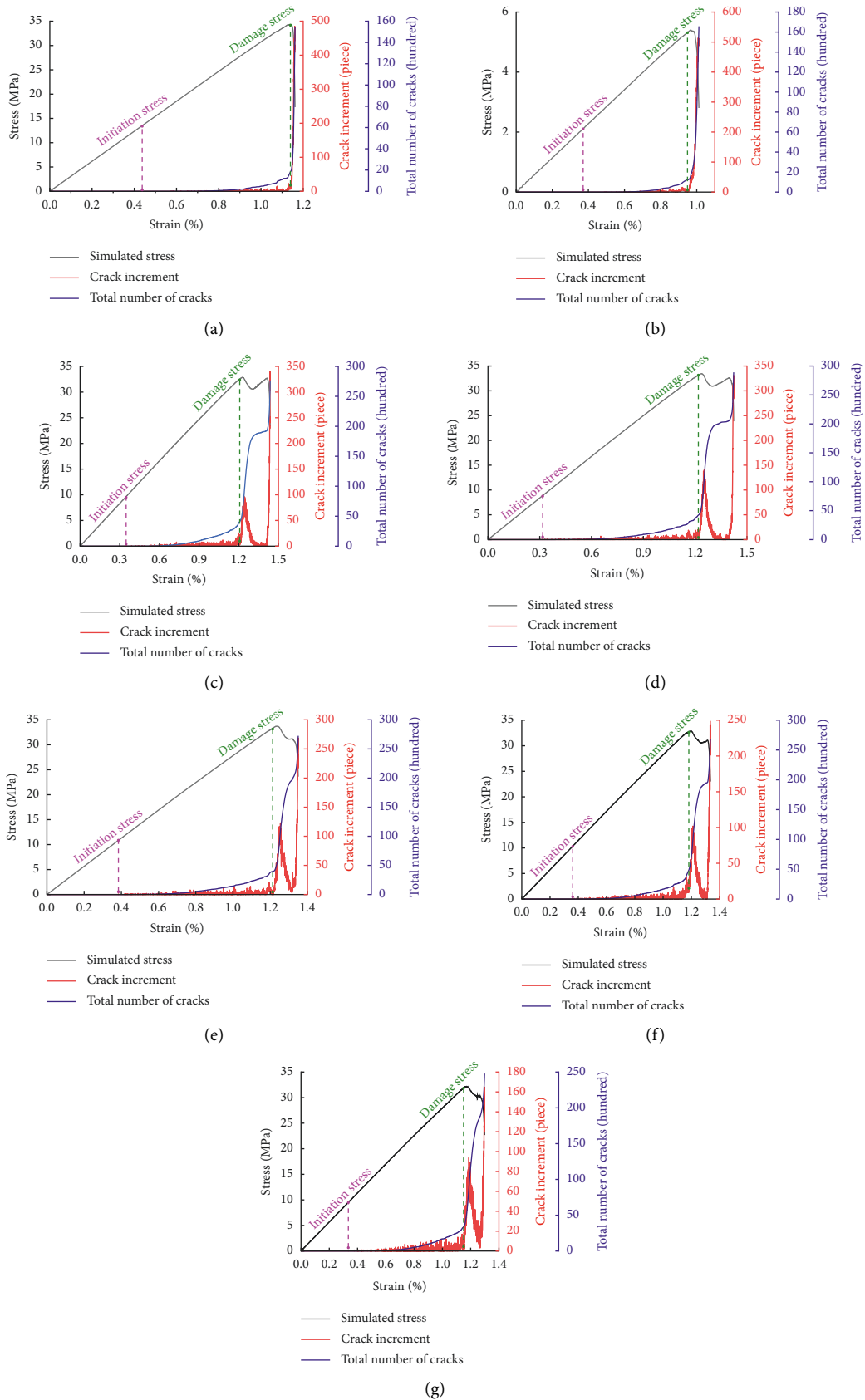
FIGURE 15: Crack evolution curves. (a) Single body artificial dam, (b) single body coal pillar, (c) 50° combined body, (d) 60° combined body, (e) 70° combined body, (f) 80° combined body, and (g) 90° combined body.

internal cracks in the combined body developed from initiation to evolution, which was followed by penetration, causing the overall structure to become unstable. The behaviors of the coal pillar-artificial dam were similar to those of the artificial dam, while the evolution of internal cracks in the coal pillar-artificial dam specimen was the same.

With the application of stress, coal pillar-artificial dam first experiences elastic strain. The contact stress between particles is less than the bonding strength between particles, and no cracks are generated inside at this time. The stress increases gradually, and the contact stress between the particles becomes greater than the bonding strength, which leads to the destruction of the bonds between the particles and the appearance of microcracks in the specimen. The number of microcracks grows rapidly until the specimen is damaged. The cracks in the specimen continue to increase after failure, showing the final failure form. The coal pillar-artificial dam specimen still has a certain degree of viscosity after reaching the compressive strength. It shows a stable period in the crack evolution curve, and the number of cracks does not increase. After the energy is released, the specimen collapses instantly with an even higher crack increase rate.

The axial stress corresponding to crack initiation is the initiation stress, and the stress corresponding to the point where the number of cracks in the coal pillar-artificial dam increases rapidly is called the damage stress. The initiation stress σ_i and damage stress σ_d of each combined body and their relationship with peak stress σ_s are shown in Table 5.

It can be seen from Figure 16 that the simulated crack initiation stress of the coal pillar-artificial dam specimen showed a trend of increasing first and then decreasing with the increase in the angle, reaching the peak value at 70°, which bore out the experimental values. Since the bonding contact stress between the particles in the artificial dam exceeded that of the coal pillar particles, the initiation stress of the artificial dam was larger than that of the coal pillar. The initiation stress of the combined body is mainly controlled by the contact stress between the filler particles. Therefore, the initiation stress of the coal pillar-artificial dam is mainly determined by the internal deformation of the coal pillar.

The test mean curve was fitted using the single peak extreme formula:

$$\sigma_i = 9.18 + 1.74e^{\left(-e^{-\dfrac{x_s - 71.76}{7.30}} - \dfrac{x_s - 71.76}{7.30} + 1\right)}, \quad (11)$$

where σ_i is the initiation stress of the simulated test piece and x_s is the interface angle of the coal pillar-artificial dam. The correlation coefficient R^2 is 0.99. The formula can characterize the influence of angle changes on crack initiation, and the occurrence of internal cracks can be predicted by observing the increase in stress.

It can be seen from Figure 17 that the increase in the angle caused the damage stress to increase first and then decrease, but both were intermediate to the single body coal pillar and the single body artificial dam. Since the damage
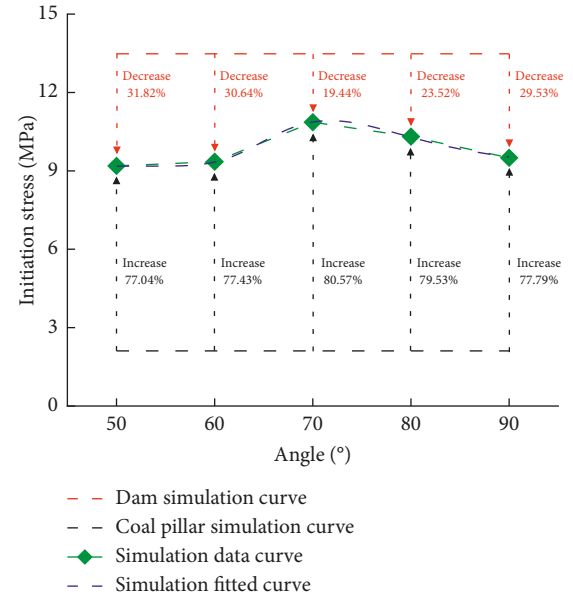

Figure 16: Relationship between angle and initiation stress.

Table 5: Crack evolution of coal pillar-artificial dam.

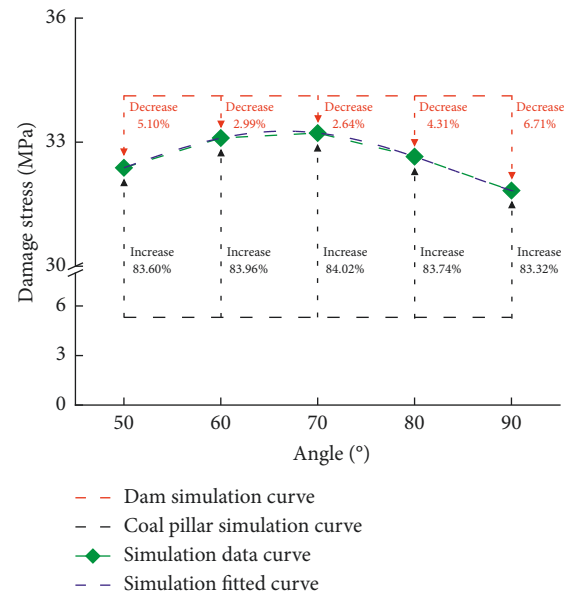| Group	Initiation stress (MPa)	Damage stress (MPa)	$\frac{\sigma_i}{\sigma_s}$ (%)	$\frac{\sigma_d}{\sigma_s}$ (%)
Dam	13.48	34.12	39.27	99.40
Coal	2.11	5.31	39.06	98.29
50°	9.19	32.38	27.97	98.56
60°	9.35	33.10	27.94	98.92
70°	10.86	33.22	32.22	98.55
80°	10.31	32.65	31.38	99.39
90°	9.50	31.83	29.50	98.86

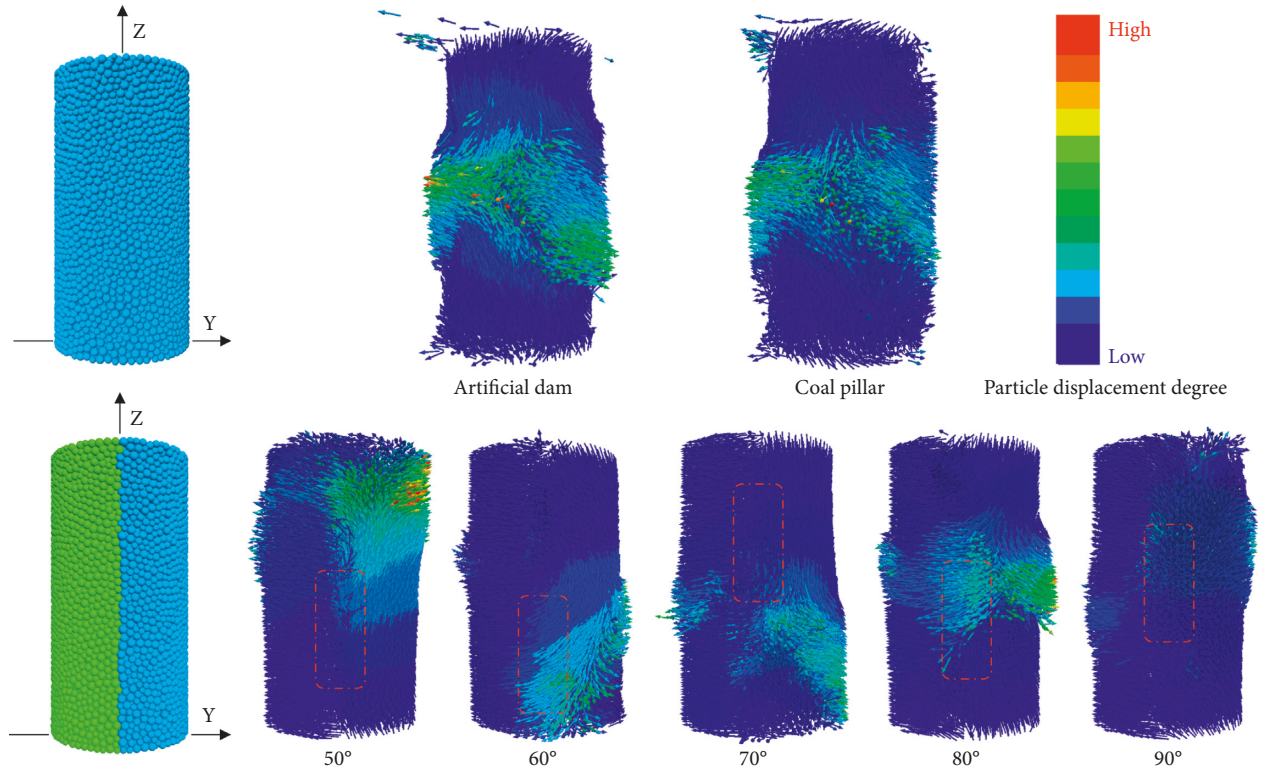Figure 17: Relationship between angle and damage stress.

FIGURE 18: Particle displacement distribution.

stress corresponds to the point of rapid growth of the number of internal cracks in the model, it implies that the bonds between the internal particles have been destroyed at this time. Therefore, it is believed that the damage stress is mainly controlled by the contact stress between the particles on the side of the artificial dam, and the damage stress to the combined body is mainly affected by the internal bonds of the artificial dam.

The test mean curve was fitted using the single-peak Gauss formula:

$$\sigma_d = 30.84 + 106.2534.91 \sqrt{\frac{\pi}{2}} e^{-2 \frac{(x_s - 66.63)^2}{34.31^2}}, \quad (12)$$

where σ_d is the damage stress of the simulated test piece and x_s is the interface angle of the coal pillar-artificial dam. The correlation coefficient R^2 is 0.99. The formula can characterize the relationship between angle change and crack evolution, and the distribution and penetration of internal cracks can be judged by observing the increase in stress.

The initiation stress and damage stress of the two-material model were both intermediate to the values associated with the coal pillar and the artificial dam single bodies, while the ratio of the initiation stress to the peak stress was smaller than the single body models. The ratio of damage stress to peak stress was intermediate to that of the coal pillar and the artificial dam. Inside the coal pillar single body model, due to the low bond strength between the particles, when cracks occur, they will rapidly expand and coalesce, resulting in macroscopic damage to the coal pillar. In the coal pillar-artificial dam model, after cracks occur, the crack

propagation and penetration speed were reduced due to the restriction of the particle bonds on the side of the artificial dam. Therefore, the macroscopic damage occurred later, which was between the coal pillar and the artificial dam single bodies.

5.2. Particle Displacement of Coal Pillar-Artificial Dam.
By observing the particle displacement on both sides of the coal pillar-artificial dam interface (Figure 18), the combined body stress state can be obtained, and the mechanical model can be judged.

The particle displacements in the single body artificial dam and the single body coal pillar were comparable. Both moved along the axis from the center to either side, and the displacement on both sides was the same. In contrast, the main displacement of the coal pillar-artificial dam combined body model was on the side of the artificial dam, and there was an obvious interface.

As the angle increases, the particle displacement changed from collision to intrusion, then to interaction, and then again to intrusion and collision, respectively, corresponding to the stress states of split bearing–sharing bearing–coordinated bearing–split bearing–sharing bearing. On the side of the artificial dam, the collisional displacement occurred both along the vertical interface and in the opposite direction, with the outward expansion displacement being dominant (50° and 90° models). The monomers on both sides are, respectively, subjected to force, and the particles expand outward under the action of the force, and collide at the interface.
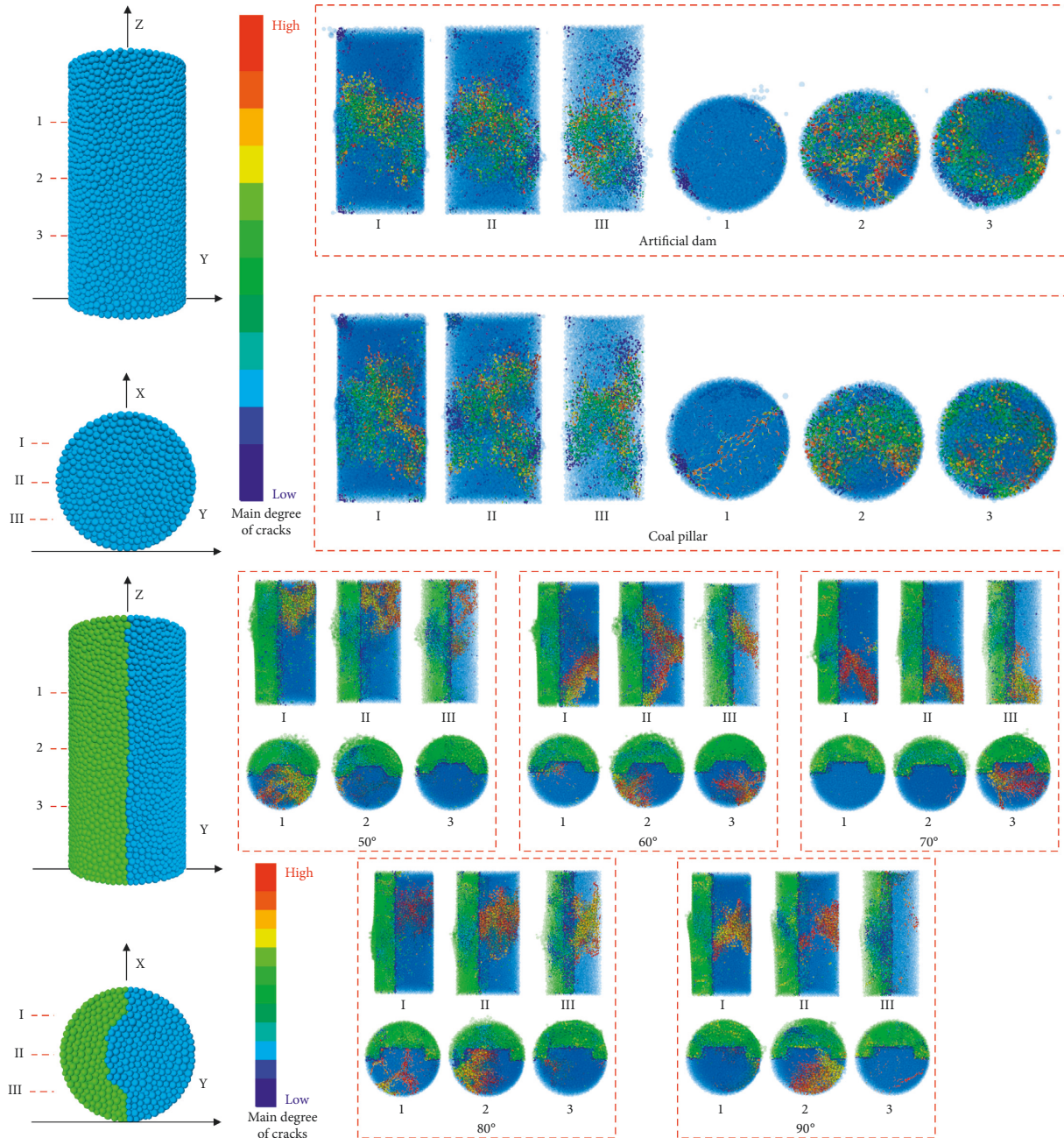
FIGURE 19: Numerical simulation of the spatial distribution of cracks.

The overall intrusive displacement was dominated by a single direction displacement, with the displacement of the coal pillar side increasing significantly (60° and 80° models). The monomer on one side is mainly stressed, and the particles move to the area with less stress, causing the intrusion of particles on one side.

The interactive displacement had strong displacement clusters on both the coal pillar side and the artificial dam side, and there was an interactive phenomenon at the interface. The particles have no obvious directionality under the action of stress, and the specimen expands outward as a whole.

5.3. Spatial Distribution of Coal Pillar-Artificial Dam Cracks.

The final failure forms of coal-pillar single body, artificial-dam single body, and coal pillar-artificial dam were analyzed. The test pieces were sliced at 25 mm, 50 mm, and 75 mm heights to analyze the development of cracks in the horizontal direction. At the same time, the axial crack distribution was obtained by slicing at 12.5 mm, 25 mm, and 37.5 mm in the transverse direction (Figure 19).

It can be seen from Figure 19 that the distribution of cracks in the single body coal pillar and the single body artificial dam specimen was relatively uniform, and the main cracks were distributed throughout the test pieces.
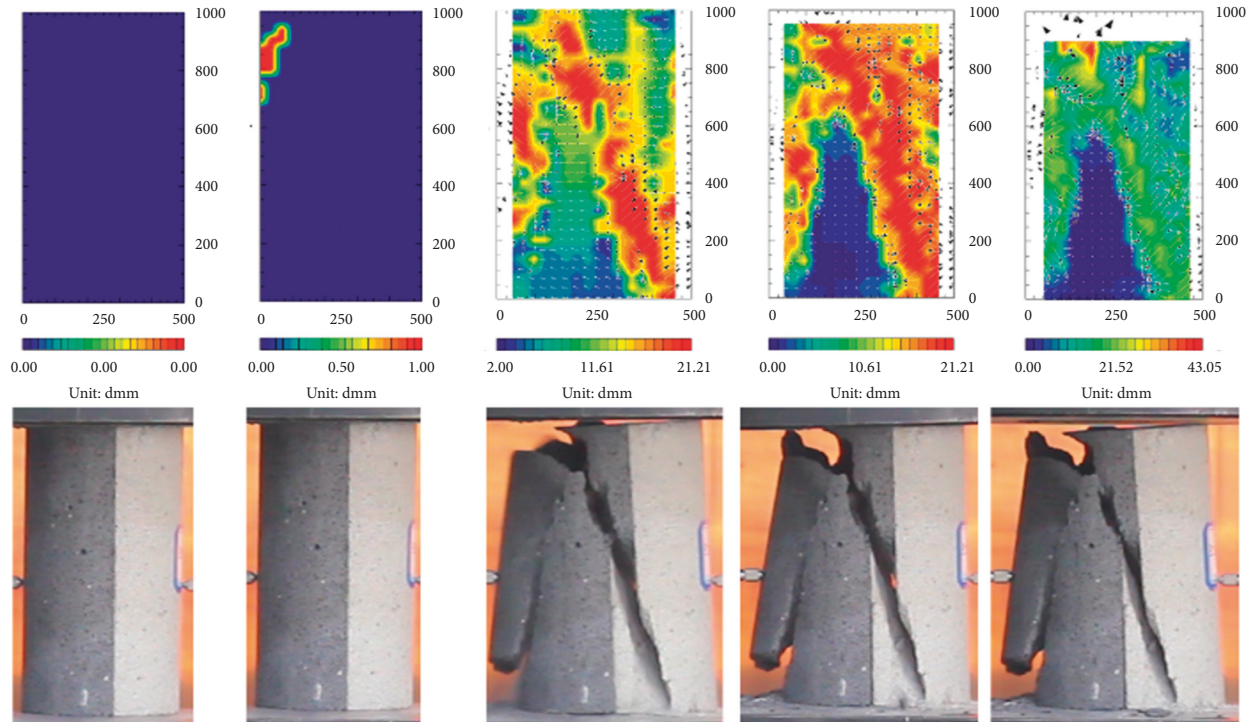
FIGURE 20: Coal pillar-artificial dam test failure forms.

Both were dominated by monoclinic splitting failure, while the evolution of individual coal pillar cracks was more complicated.

The cracks in the coal pillar-artificial dam combined body model were clearly demarcated along the interface. The main cracks of the specimen were concentrated on the artificial dam side with a clustered distribution, while the cracks on the coal pillar side were relatively scattered and basically covered the entire coal pillar area. At the same time, as the inclination increased, the position of the main cracks gradually shifted downwards and then upwards, and the macroscopic particle splashing also followed this trend. The damage of coal pillar-artificial dam was still dominated by monoclinic splitting. Taking the damage test of a 70° specimen as an example (Figure 20), the simulation and the test macroscopic damages were the same.

6. Conclusion

(1) Judging by the tightness of the bonding between the coal pillar and the artificial dam, the stress state can be divided into three types: split bearing, shared bearing, and coordinated bearing, corresponding to three different constitutive models.

(2) The test stress–strain curve had five stages, while the combined-body simulation curve showed an obvious postpeak viscosity. The compressive strength and mean peak strain curve for the coal pillar model showed a single-peak change trend that first increased and then decreased, and the peak value exceeded the compressive strength of the single body specimen of the artificial dam.

(3) The total energy and elastic energy of coal pillar-artificial dam under load showed the same trend. The dissipation energy curve showed an obvious increase in the early stage, then tended to flatten, and finally decayed. With the change in angle, the dissipation energy curve of the combined body specimen showed a unimodal trend of increasing first and then decreasing.

(4) The simulated initiation stress and damage stress of the coal pillar-artificial dam test piece were intermediate to the coal pillar and artificial dam single bodies. At the same time, with the increase in inclination, it showed a trend of increasing first and then decreasing, reaching a peak at 70°. The crack propagation and penetration speed were limited by the particle bonding on the artificial dam side.

(5) As the angle increased, the particle displacement of coal pillar-artificial dam model was collision–intrusive–interactive–intrusive–collision, corresponding to the stress state of split bearing–shared bearing–coordinated bearing–split bearing–shared bearing.

(6) Failure mechanism in both the single-body and combined body models was dominated by monoclinic splitting. The cracks of the coal pillar-artificial dam combined body model were clearly demarcated along the interface. The main cracks of the specimen were concentrated on the side of the artificial dam with a clustered distribution. At the same time, as the angle increased, the position of the main cracks gradually shifted downwards and then upwards [27, 30, 31].

Data Availability

The data used to support the findings of this study are included within the article.

Disclosure

This article was published as a preprint based on the link: https://assets.researchsquare.com/files/rs-929950/ v1_covered.pdf?c = 1632931903"c = 1631877758.

Conflicts of Interest

The authors declare no conflicts of interest.

Acknowledgments

References

[1] L. Yuan and K. Yang, "Further discussion on the scientific problems and countermeasures in the utilization of abandoned mines," *Journal of China Coal Society*, vol. 46, no. 1, pp. 16–24, 2021.

[2] G. H. XieYQ and LiC. SuZG, "Exploitation and utilization of renewable energy from waste mine resources," *Renewable Energy Resources*, vol. 38, no. 3, pp. 423–426, 2020.

[3] C.W. J. LiuF, C.G. M. ZhangJM, and L. F Guo, "Current technological innovation and development direction of the 14th five-year plan period in China coal industry," *Journal of China Coal Society*, vol. 46, no. 1, pp. 1–15, 2021.

[4] J.Y. D. YuanL, Z.Y. X. WangK, and XuC. HaoXJ, "Precision exploitation and utilization of closed/abandoned mine resources in China," *Journal of China Coal Society*, vol. 43, no. 1, pp. 14–20, 2018.

[5] G.M. Z. XieHP, Z. R. GaoF, XuH. JuY, and Y. W Wang, "Strategic conceptualization and key technology for the transformation and upgrading of shut-down coal mines," *Journal of China Coal Society*, vol. 42, no. 6, pp. 1355–1365, 2017.

[6] B.Z. F. PuH and XuJ. C. ZhangJX, "Research on a reuse mode of geothermal resources in abandoned coal mines," *Journal of China Coal Society*, pp. 1–11, 2021.

[7] H.Z. M. XieHP, Z. L. GaoF, and Y. N. Gao, "A new technology of pumped-storage power in underground coal mine: principles, present situation and future," *Journal of China Coal Society*, vol. 40, no. 5, pp. 965–972, 2015.

[8] GuD. Z. LiT, D.B. Q. LiJF, and S. Q Liu, "Construction of pumped storage peak shaving system for mine water based on abandoned coal mine goaf," *Coal Science and Technology*, vol. 46, no. 9, pp. 93–98, 2018.

[9] F.Y. H. SuiS and Z.X. L. LiM, "Construction and application of evaluation system for operation effect of underground reservoir," *China Journal of Oceanology*, vol. 50, no. 6, pp. 126–133, 2020.

[10] R. Esmaeil, M. Ehsan, S. Reza, and G. Mehran, "Optimized algorithm in mine production planning, mined material destination, and ultimate pit limit," *Journal of Central South University*, vol. 25, no. 6, pp. 1475–1488, 2018.

[11] D. Z. Gu, "Theory framework and technological system of coal mine underground reservoir," *Journal of China Coal Society*, vol. 40, no. 2, pp. 239–246, 2015.

[12] F. Liu and S. Z. Li, "Discussion on the new development and utilization of underground space resources of transitional coal mines," *Journal of China Coal Society*, vol. 42, no. 9, pp. 2205–2213, 2017.

[13] T. B. Zhao, M. L. Xing, W. Y. Guo, C. W. Wang, and B. Wang, "Anchoring effect and energy-absorbing support mechanism of large deformation bolt," *Journal of Central South University*, vol. 28, no. 2, pp. 572–581, 2021.

[14] Z. G. Cao, "Study on aseismic performance of different artificial dam structures of coal mine underground reservoir," *Coal Science and Technology*, vol. 48, no. 12, pp. 237–243, 2020.

[15] P. Peng, Z. G. Shan, and Y. F. Dong, "Coupling model for assessing anti-seepage behavior of curtain under dam foundation," *Journal of Central South University*, vol. 19, no. 7, pp. 2016–2021, 2012.

[16] Q. L. Yao, Y. P. Liu, T. Chen, X. H. Li, S. Y. Yang, and H. F. Duan, "Experimental study of damage evolution of artificial dam strength of underground reservoir," *Journal of China Coal Society*, vol. 43, no. 4, pp. 1111–1117, 2018.

[17] D. Z. Gu, Y. G. Yan, Y. Zhang, E. Z. Wang, and Z. G. Cao, "Experimental study and numerical simulation for dynamic response of coal pillars in coal mine underground reservoir," *Journal of China Coal Society*, vol. 41, no. 7, pp. 1589–1597, 2018.

[18] S. Y. Wang and H. Y. Zuo, "Safety diagnosis on coal mine production system based on fuzzy logic inference," *Journal of Central South University*, vol. 19, no. 2, pp. 477–481, 2012.

[19] Q. M Huang, S. M Liu, W. M Cheng, and G. Wang, "Fracture permeability damage and recovery behaviors with fracturing fluid treatment of coal: an experimental study," *Fuel*, vol. 282, p. 118809, 2020.

[20] X Xu, L. Zhou, and Q. Y Feng, B Gao, Research progress of gas-water-rock interaction for gas occurrence and migration in abandoned coal mine," *Safety in Coal Mines*, vol. 47, no. 6, pp. 1–4, 2016.

[21] B. B. Wang, B. Liang, J. G. Wang, K. M. Sun, W. J. Sun, and H. B. Chi, "Experiment study on rock bulking of coal mine underground reservoir," *Rock and Soil Mechanics*, vol. 39, no. 11, pp. 4086–4092+4101, 2018.

[22] J. Z. Tang, S. Q. Yang, D. Elsworth, and Y. Tao, "Three-dimensional numerical modeling of grain-scale mechanical behavior of sandstone containing an inclined rough joint," *Rock Mechanics and Rock Engineering*, vol. 54, no. 2, pp. 905–919, 2020.

[23] C. Zhang, P. H. Han, F. T. Wang, and X. He, "The stability of residual coal pillar in underground reservoir with the effect of mining and water immersion," *Journal of China University of Mining and Technology*, pp. 1–8, 2021.

[24] T. R. Ma, D. P. Ma, and Y. J. Yang, "Fractal characteristics of coal and sandstone failure under different unloading confining pressure tests," *Advances in Materials Science and Engineering*, 2020.

[25] JuJ. F. BaiDY and LiJ. H. XuJL, "Stability analysis of mine underground reservoir artificial dam in Lijiahao mine," *Journal of China Coal Society*, vol. 42, no. 7, pp. 1839–1845, 2017.

[26] B. F. Wang, L. Wu, J. Zhang, B. Liang, and C. B. Liu, "Experiment on size effect for deformation characteristics of rock and coal in coal mine underground reservoir," *Journal of Mine Safety and Engineering*, pp. 1–10, 2021.

[27] Q. L. Yao, Q. Hao, X. Y. Chen, B. J. Zhou, and J. Fang, "Design on the width of coal pillar dam in coal mine groundwater reservoir," *Journal of China Coal Society*, vol. 44, no. 3, pp. 891–899, 2019.

[28] P. X. Zhao, Y. C. He, S. G. Li, H. F. Lin, Y. Y. Jia, and E. H. Yang, "Coal thickness effect on mechanics and energy characteristics of coal-rock combination model," *Journal of Mine Safety and Engineering*, vol. 37, no. 5, pp. 1067–1076, Article ID 106445, 2020.

[29] C. J. Li, Y. Xu, M. M. Feng, and B. Pan, "Deformation law and failure mechanism of coal-rock-like combined body under uniaxial loading," *Journal of China Coal Society*, vol. 45, no. 5, pp. 1773–1782, 2020.

[30] F. Du, K. Wang, X. L. Dong, and J. P. Wei, "Numerical simulation of damage and failure of coal-rock combination based on CT three-dimensional reconstruction," *Journal of China Coal Society*, pp. 1–12, 2021.

[31] Y. Rui, J. K. Lv, Z. Bo, and D. P. Ma, "Rock unloading failure precursor based on acoustic emission parametric fractal characteristics," *Lithosphere*, vol. 2022, 2020.

[32] K. Yang, W. J. Liu, L. T. Dou, X. L. Chi, Z. Wei, and Q. Fu, "Experimental investigation into interface effect and progressive instability of coal-rock combined specimen," *Journal of China Coal Society*, vol. 45, no. 5, pp. 1691–1700, 2020.

[33] Z. Y. Fang, J. F. Ju, Z. G. Cao, X. Z. Wang, and J. L. Xu, "Numerical simulation of damage and failure of coal-rock combination based on CT three-dimensional reconstruction," *Journal of China Coal Society*, pp. 1–12, 2021.

[34] M. K. Duan, C. B. Jiang, W. M. Yin, K. Yang, J. Z. Li, and Q. J. Liu, "Experimental study on mechanical and damage characteristics of coal under true triaxial cyclic disturbance," *Engineering Geology*, vol. 295, Article ID 106445, 2021.

[35] Z. Li and Q. H. Rao, "Quantitative determination of PFC3D microscopic parameters," *Journal of Central South University*, vol. 28, no. 3, pp. 911–925, 2021.

[36] K. Yang, X. Lyu, Q. P. Liu et al., "Experimental study on instability characteristics of coal pillar-artificial dam bond in abandoned mine," *J Min Safety Eng*, pp. 1–16, 2022.

[37] X. Lyu, K. Yang, J. J. Fang, Z. N. Zhang, Y. Wang, and Q. Fu, "Simulation of the uniaxial mechanical properties and crack evolution of coal pillar-artificial dam in abandoned mines," *Journal of China Coal Society*, 2021.